Review of Scientific Instruments

RESEARCH ARTICLE | MAY 09 2025

Droplet heterogeneous nucleation in a rapid expansion aerosol chamber

Martin A. Erinin ; Cole R. Sagan ; Ilian Ahmed ; Gwenore F. Pokrifka ; Nadir Jeevanjee ; Marissa L. Weichman ; Luc Deike

Check for updates

Rev. Sci. Instrum. 96, 055104 (2025)
https://doi.org/10.1063/5.0255658

View Online
Export Citation

Articles You May Be Interested In

Development and validation of a new cloud simulation experiment for lab-based aerosol–cloud studies

Rev. Sci. Instrum. (September 2022)

09 May 2025 20:58:15

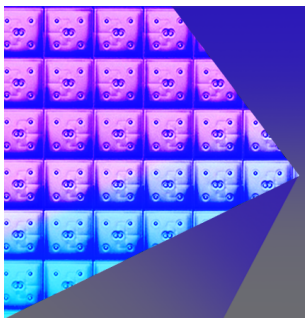

Review of Scientific Instruments

Special Topics Now Online

Learn More

AIP Publishing

AIP Publishing

Review of Scientific Instruments ARTICLE pubs.aip.org/aip/rsi

Droplet heterogeneous nucleation in a rapid expansion aerosol chamber

Cite as: Rev. Sci. Instrum. 96, 055104 (2025); doi: 10.1063/5.0255658
Submitted: 30 December 2024 • Accepted: 21 April 2025 •
Published Online: 9 May 2025

View Online Export Citation CrossMark

Martin A. Erinin,[1] Cole R. Sagan,[2] Ilian Ahmed,[1,3] Gwenore F. Pokrifka,[4] Nadir Jeevanjee,[5] Marissa L. Weichman,[2] and Luc Deike[1,4,a)]

AFFILIATIONS

[1] Department of Mechanical and Aerospace Engineering, Princeton University, Princeton, New Jersey 08540, USA
[2] Department of Chemistry, Princeton University, Princeton, New Jersey 08540, USA
[3] Département de Physique, École Normale Supérieure de Paris, Paris, France
[4] High Meadows Environmental Institute, Princeton University, Princeton, New Jersey 08544, USA
[5] Geophysical Fluid Dynamics Laboratory, NOAA, Princeton, New Jersey 08540, USA

[a)] **Author to whom correspondence should be addressed:** ldeike@princeton.edu

ABSTRACT

We present a new experimental facility to investigate the nucleation and growth of liquid droplets and ice particles under controlled conditions and characterize processes relevant to cloud microphysics: the rapid expansion aerosol chamber (REACh). REACh is an intermediate size chamber (~0.14 m^3) combining the principle of an expansion chamber with the ability to probe the influence of turbulent flows. Water droplet heterogeneous nucleation onto seeding aerosols is achieved via a sudden pressure drop accompanied by a temperature drop, which can cause humid air to condense into a cloud of droplets under appropriate thermodynamic conditions. REACh features tight control and monitoring of the initial saturation ratio of water vapor, identity and concentration of seeding aerosol particles, temperature, pressure, and air flow mixing, together with high speed real-time measurements of aerosol and droplet size and number. Here, we demonstrate that the minimum temperature reached during each expansion can be reasonably described by the thermodynamics of dry or moist adiabats for a range of initial relative humidities. The size and number of droplets formed and the overall lifetime of the cloud are characterized as a function of the aerosol concentration and initial water vapor saturation ratio. The total droplet concentration scales linearly with the seeding aerosol concentration, suggesting that all injected aerosol particles serve as condensation nuclei. While the total number of droplets formed increases with aerosol concentration, the mean droplet size decreases with the concentration of seeding aerosols as a result of competition for the available water vapor. Theoretical considerations provide a quantitative prediction for the mean droplet size over a range of conditions. The high repetition rate of experiments that we can perform with the REACh facility will permit extensive characterization of aerosol processes, including droplet and ice nucleation onset and growth, and the importance of turbulence fluctuations. We will leverage the capabilities of this facility to explore a wide range of physical parameters encompassing regimes relevant to cloud microphysics.

© 2025 Author(s). All article content, except where otherwise noted, is licensed under a Creative Commons Attribution (CC BY) license (https://creativecommons.org/licenses/by/4.0/). https://doi.org/10.1063/5.0255658

09 May 2025 20:58:15

I. INTRODUCTION

One of the largest remaining uncertainties in climate projections involves the impact of aerosols on the optical properties of clouds.[1] Aerosols are particles suspended in the atmosphere that can serve as cloud condensation nuclei (CCN) upon which water vapor can condense to form cloud droplets. Understanding the influence of different seeding aerosols on aerosol activation (i.e., water droplet nucleation), droplet growth, and evaporation is essential for accurate predictions of cloud behavior and resulting impacts on the environment.[2–4]

The relevant physical scales for warm clouds composed of liquid droplets span several orders of magnitude, ranging from nano-scale aerosol particles [$\mathcal{O}$(10 nm)], to micro-scale droplets [$\mathcal{O}$(10 μm)], to small-scale turbulent fluctuations [$\mathcal{O}$(cm)], to meso-scale turbulent processes such as cloud top entrainment [$\mathcal{O}$(1–10 m)], and to large-scale convective patterns [$\mathcal{O}$(1–10 km)]. The nucleation of cloud droplets and their subsequent growth

© Author(s) 2025

dynamics lead to specific concentrations and size distributions of droplets, depending on the seeding aerosol number density and composition, and the thermodynamic conditions of the surrounding environment (e.g., water vapor concentration, temperature, and pressure), which are themselves modulated by the surrounding turbulent flow.[5–7] These factors determine whether cloud droplets remain stable for extended periods of time or rain out and also govern the optical interactions of the droplets with sunlight and terrestrial radiation.[4,8]

Beyond the challenges of droplet nucleation in warm turbulent clouds, higher latitude low level clouds can be mixed-phase, containing both crystalline ice and liquid water droplets,[9,10] which add further complexity to aerosol nucleation microphysics. At higher altitudes, cirrus clouds and contrails are formed purely of ice particles. The conditions under which ice-nucleating particles form and the size and shape of atmospheric ice crystals are particularly sensitive to the size and chemical composition of seeding aerosol nuclei.[9,11,12] There are also many open questions regarding the sensitivity of ice formation to thermodynamic conditions and the interplay between homogeneous freezing and various modes of heterogeneous freezing on seeding aerosol.[9,11]

Despite decades of laboratory efforts, observational field studies, remote sensing, and modeling work, fundamental questions remain regarding the nucleation and growth of droplets and ice on aerosols. These processes play a critical role in atmospheric science, through their influence on cloud processes, weather patterns, and radiative balance of Earth's atmosphere,[1] and are central to proposed climate mitigation strategies such as marine cloud brightening[13] and cirrus cloud thinning.[14]

Highly controlled laboratory conditions provide a path forward to gain physical insights into the mechanisms responsible for ice and droplet nucleation on seeding aerosols and subsequent growth under various thermodynamical conditions. While experimental cloud chambers have been instrumental in developing the understanding of cloud microphysics and informing parameterizations implemented in large-scale models,[4,15–18] only a few chambers are still in operation.[19] As discussed by Shaw *et al.*,[19] there is a significant need for a renewed effort of experimental studies into cloud and aerosol microphysics in controlled environments (i.e., well-constrained boundary conditions, thermodynamical properties, seeding aerosol ensembles, and turbulence conditions). The ideal cloud chamber experiment should include diagnostics capable of detecting multiscale dynamics directly within the flow, including droplet and ice particle size and spatial distributions as well as water vapor content. The ability to isolate specific processes is essential, as is a high degree of repeatability, in order to make detailed comparisons between experiments and modeling frameworks.

Cloud chambers can operate through different working principles, two configurations being expansion (Wilson-type) chambers and turbulent convection chambers. To give two relevant examples, the Aerosol Interaction and Dynamics in the Atmosphere (AIDA) expansion chamber at the Karlsruhe Institute of Technology (KIT)[20] and the turbulent Π cloud chamber at Michigan Technological University (MTU)[6,21] have contributed to recent scientific discoveries on aerosol cloud microphysics.

The AIDA facility is a large volume (84 m^3) expansion chamber capable of studying droplet and ice growth over a range of thermodynamic conditions.[20] The large chamber size brings certain operational challenges and motivated KIT to develop a smaller (0.02 m^3) vessel, AIDAm, housed inside AIDA. AIDAm is used to study the long-term physical and chemical aging of aerosols under relevant atmospheric thermodynamic conditions and to measure the impact of aging on aerosol ice-nucleating properties.[22] The Portable Ice Nucleation Experiment (PINE) chamber[23] is another expansion chamber led by KIT, designed as a plug and play facility. PINE is capable of minute-to-hour-long observations of ice-nucleating particles by controlling the wall temperatures and thereby creating the necessary thermodynamic conditions for ice growth. PINE's small volume (0.01 m^3) and portable design permits its deployment in field sites[24] allowing for monitoring ice nucleation on aerosols in various atmospheric backgrounds. Small-scale expansion chambers in various other locations have also been used to study heterogeneous gas-to-liquid phase transitions for various particles and vapors, including investigations into droplet heterogeneous nucleation in microgravity[25] and heterogeneous nucleation of water vapor[26] and water–*n*-propanol[27] mixtures on silver nanoparticles.

In an alternative mode of operation, the Π chamber at MTU uses Rayleigh–Bénard turbulent convection conditions to study aerosol–cloud interactions, cloud formation, and turbulence coupling.[6,21] Elegantly, specific humidity and temperature boundary conditions may be chosen to reach supersaturation inside the chamber, leading to droplet heterogeneous nucleation. The Π chamber is meter-scale (volume of 3.14 m^3) and operates in a statistically stationary state with a continuous injection of aerosols to compensate for sedimentation and wall loss. Studies of droplet formation and dynamics over minutes to days have been performed, with a focus on droplet–turbulence interactions. Major efforts have analyzed preferential sampling,[28] the heterogeneous spatial distribution of cloud droplets,[29] and the effect of fluctuating saturation fields in turbulent clouds.[6]

Following a recent community workshop, Shaw *et al.*[19] laid out a list of lingering open questions in cloud microphysics and the experimental scales needed to address them. While a very tall convection chamber is required for some questions—including rain formation and processes at the cloud boundary where gradients are sharp—meter-scale chambers are sufficient to attack key questions on aerosol activation, droplet formation and growth, and ice formation and growth. Small centimeter-scale chambers have been used in single-particle growth studies and have revealed a diversity of ice growth behaviors that may be impossible to directly observe in a large AIDA-scale chamber.[30–32] Intermediate-scale cloud chambers are more suitable to measure the diversity of ice growth within a population of particles. Smaller facilities also have the advantages of easier logistics and faster experimental repetition rates, making them possible to sweep a wider range of conditions in a fixed amount of lab time. The facility we introduce in this paper has been specifically designed to target such questions.

Here, we present a new intermediate-scale cloud-chamber facility: the rapid expansion aerosol chamber (REACh). REACh consists of two vacuum chambers: a 0.14 m^3 aerosol chamber, where seeding aerosols are introduced and measurements are conducted, and the expansion chamber, into which the aerosol chamber can be vented to create the necessary conditions for droplet (or ice) nucleation. Crucially, our setup allows for a very fast repetition rate, with a typical

09 May 2025 20:58:15

© Author(s) 2025

expansion experiment taking only ~30 min to set up and run. We can survey a wide range of aerosol, flow, and thermodynamic conditions in just a few days. Such fast experimental turnaround times can be intractable in larger chambers. This facility also includes the possibility to introduce turbulent flow during the expansion—inspired from particles in turbulence studies[5,33,34]—so that droplet and ice nucleation and growth can be studied in a fluctuating environment.

The REACh facility emphasizes a suite of high-frequency, accurate diagnostic methods to monitor droplet growth and thermodynamical conditions throughout each expansion experiment. Detailed quantification of droplet properties is enabled by the use of phase Doppler anemometry (PDA), high-speed in-line holography,[35–37] and temporally resolved measurements of the chamber temperature and pressure. An infrared absorption spectroscopy system to measure the saturation ratio has also been implemented and will be presented in a follow-up paper. Such real-time measurements are essential to advance the understanding of cloud microphysics. Nucleation diagnostics are often made post-hoc, e.g., by extracting samples from the chamber and running subsequent analyses. Such methods result in the loss of timescale information needed to constrain particle and cloud growth models. Our more ideal diagnostics track the size distribution and number densities of dry aerosols and droplets together with temperature and liquid vapor content[38] and the spatial and temporal fluctuations of these fields.

In this paper, we demonstrate the capabilities of the REACh facility for the parametric studies of the heterogeneous nucleation and growth of liquid droplets. In particular, we consider water droplet nucleation on pre-existing aerosol intentionally introduced into the chamber and the subsequent growth of these liquid droplets. We refer to this process hereafter as "water droplet nucleation (on an aerosol)" for brevity. We do not consider the formation of particles/drops directly from the vapor phase in the present work. The kinetics of droplet nucleation and growth are not typically considered in atmospheric models, yet these processes are highly relevant to the atmospheric behavior of large aerosol particles (e.g., sea-salt) that might be used in hygroscopic cloud seeding or marine cloud brightening.

Here, we make use of time-synchronized, highly temporally resolved measurements to probe the dynamics of the droplet growth for a variety of initial conditions, including saturation ratio, seeding aerosol concentration, and air mixing. We perform experiments that can go beyond classic atmospheric conditions in terms of particle concentration, level of supersaturation ratio, timescale of expansion, and intensity of turbulence, which can also help models avoid the extrapolation of parameters when at the edge of typical, or extreme, atmospheric conditions. We carry out these extensive parameter sweeps with the goal to gain insights into cloud microphysics and eventually inform more accurate theoretical models.

Here, we illustrate the capabilities of our rapid-expansion-cloud-chamber on the heterogeneous nucleation of liquid droplets. We make use of time-synchronized, highly temporally resolved measurements to probe the dynamics of the droplet growth for a variety of initial conditions, including saturation ratio, seeding aerosol concentration, and air mixing.

The remainder of this paper is organized as follows: We describe the operating principle of the facility, experimental procedures, measurement instrumentation, and facility characterization in Sec. II. We illustrate the capabilities of the system by characterizing the thermodynamics and associated droplet heterogeneous nucleation and growth in various aerosol concentration regimes in Sec. III, with dense regimes of droplets characterized by PDA and dilute regimes characterized by holography. We examine how droplet lifetimes, mean diameters, and concentrations

09 May 2025 20:58:15

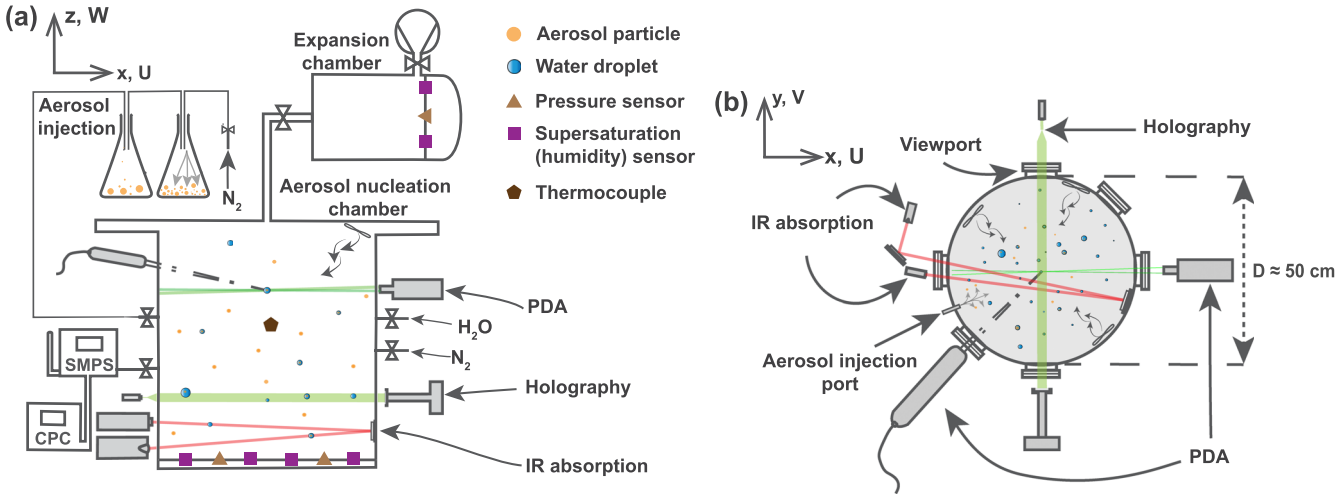

FIG. 1. Schematics of the rapid expansion aerosol chamber (REACh). (a) Side view of the aerosol-nucleation and expansion chambers along with instrumentation and control devices, including the aerosol injection system, a scanning mobility particle sizer (SMPS), a condensation particle counter (CPC), a phase Doppler anemometry (PDA) system, an inline holography system, an infrared absorption beamline, pressure sensors, thermocouple temperature sensors, and humidity sensors. (b) Top view of the aerosol-nucleation chamber and the layout of several optical instrumentation systems and viewports. Inline holography can be used to measure droplet concentrations, diameters, and speeds. Infrared (IR) absorption spectroscopy can be used to measure the partial pressure of water vapor.

© Author(s) 2025

vary as a function of initial saturation ratio and aerosol concentration. We provide conclusions and a future outlook in Sec. IV.

II. EXPERIMENTAL METHODS

A. Experimental apparatus and procedure

Figure 1 shows a schematic of the REACh facility. Engineering drawings are included in the supplementary material. Both the aerosol-nucleation and expansion chambers, as well as various control devices and diagnostics, are depicted. The facility consists of two cylindrical vacuum-sealed stainless steel (grade 304L) chambers separated by a solenoid valve, which is typically closed. The primary aerosol-nucleation chamber is where all the experimental measurements are conducted and where most of the scientific instrumentation is located. The expansion chamber is approximately equal in volume to the aerosol-nucleation chamber. We vent the contents of the aerosol-nucleation chamber into the expansion chamber to increase the saturation ratio via adiabatic expansion and cooling, thus creating conditions for droplet nucleation.

The aerosol-nucleation chamber is 50.8 cm in diameter and 49.5 cm in height with a volume of $\mathscr{V} \approx 0.14$ m^3. The volume is slightly greater than that of a cylinder due to the presence of the viewports. A vacuum-sealed access lid is located on top of the chamber, allowing easy access to the main compartment. The chamber features six 13.5 cm (5.32 in.) diameter borosilicate glass viewports positioned along its circumference to provide optical access. In addition, measurement and control devices are attached to several 20.3 cm (8 in.) and 6.99 cm (2.75 in.) access ports positioned around the circumference of the aerosol-nucleation chamber and on the top lid. The chamber walls are equipped with cooling channels, which are not used in the present work, but will permit us to explore lower-temperature conditions in the future. Three 82 mm diameter fans (CUI Devices, model CFM-9225V-130-340) are mounted onto the walls of the aerosol-nucleation chamber to enhance mixing inside the chamber. The fans are offset by 120° around the circumference of the chamber, positioned near the top and pointing toward the chamber center.

We produce a cloud of liquid droplets in the aerosol-nucleation chamber using the following procedure. First, the aerosol-nucleation chamber is prepared with the desired initial saturation ratio, S_0, and the concentration of seeding aerosols, C_0 (see Sec. II B). At the same time, the expansion chamber is evacuated to pressures as low as 2.6×10^{-5} bar using a Roots vacuum pump (Leybold ECODRY 40 plus). Fully pumping down the expansion chamber results in a maximum pressure drop in the aerosol-nucleation chamber of $\Delta p = 0.54$ bar upon venting; this is the condition used for the majority of experimental runs reported in this paper. As described in Sec. III A, we can also work with a smaller pressure drop by only partially evacuating the expansion chamber.

An experiment is initiated when the solenoid valve connecting the two chambers is opened rapidly (~20 ms opening time), causing gas to flow out of the aerosol-nucleation chamber in ~0.5 s. Note that the rate of expansion can be controlled via the solenoid valve, although we do not explore this degree of freedom in the present experiments. Changing expansion timescales would also need to be associated with wall temperature control. This expansion drops the aerosol-nucleation chamber pressure and is accompanied by a drop in temperature and a corresponding increase in saturation ratio (see the next paragraph). At this point, water droplets may begin to form in the aerosol-nucleation chamber. Nucleation can, in principle, occur either via heterogeneous nucleation on seeding aerosols or via homogeneous nucleation, depending on the initial conditions. Expansion experiments can be performed with fans off (hereafter referred to as the unforced mixing case) or with the fans running (referred to as the forced mixing case) to evaluate the influence of mixing on droplet formation. Note that for all experiments in this paper, we do not observe or have direct evidence that the fans act as droplet impactors, thereby reducing the concentration of droplets in the chamber. We also note that in the current work, the rapid expansions we perform (0.54 bar pressure drops in 0.5 s) correspond to effective vertical velocities much faster than atmospheric processes. Our experiment design is not aimed to replicate the atmospheric vertical velocity but instead to obtain highly repeatable conditions, under which droplet nucleation and growth on reasonable experimental timescales are studied and a wide range of aerosol and thermodynamic parameters are probed.

One of the key metrics that governs droplet nucleation in humid air is the saturation ratio, defined as $S = e/e^*(T)$, where e is the partial pressure of water vapor and $e^*(T)$ is the saturation water vapor pressure at temperature T. S is related to the relative humidity (RH) by $S = \mathrm{RH}/100$. A large range of maximum supersaturations $(S - 1)$ can be achieved during our expansion experiments depending on the initial conditions and pressure drop.

The following data are collected for each expansion experiment: initial temperature, pressure, and saturation ratio; initial aerosol concentration; time-resolved pressure and temperature drop; and time-resolved droplet diameter, number, vertical, and horizontal speed distributions.

The aerosol-nucleation chamber pressure, temperature, and saturation ratio are monitored using the following sensors:

- Three pressure sensors (Keller Preciseline)—two in the aerosol-nucleation chamber and one in the expansion chamber—are used to measure the changes in pressure that occur during an expansion. These sensors feature a sampling rate of 250 Hz and equivalent response times.
- One thermocouple temperature sensor (Type T, 44 AWG, Omega Engineering Inc.) is hung in the center of the aerosol-nucleation chamber to measure the temperature throughout each expansion. The response time of the thermocouple is on the order of 10 ms. A cold junction compensation held at 20 °C (National Instruments SCB-68A) is applied to the thermocouple. Note that in some of the data presented here, the cold junction compensation of 20 °C was applied in post-processing. Note that the thermocouple wire is very fine and thus may move in the presence of turbulence.
- Six relative humidity sensors (Sensirion SEK-SHT35)—four near the bottom of the aerosol-nucleation chamber and two in the expansion chamber—are used to record relative humidity. The response time of these sensors is on the order of 2 s, so they are only used to record humidity before and after the expansion.

In addition to the above, we record the partial pressure of water inside the aerosol-nucleation chamber using infrared laser absorption spectroscopy.[38,39] While we do not report the results

09 May 2025 20:58:15

© Author(s) 2025

of these measurements here, we mention this technique here for completeness.

The instrumentation used to record aerosol and droplet statistics is described in Secs. II C and II D.

B. Chamber initialization

We prepare for an expansion experiment by initializing the aerosol-nucleation chamber. The most important parameters to control are the initial saturation ratio, S_0, and the concentration of dry seeding aerosol particles, C_0. It can take 20–35 min to prepare the chamber, depending on conditions.

First, we thoroughly clean both chambers of aerosols from any previous experiments. The cleaning procedure is as follows: the inside of both chambers is dusted off with compressed air, and then, the inside surfaces are cleaned with isopropyl alcohol and lint-free wipes. Finally, the chambers are sealed and evacuated, and the valve connecting the two chambers is closed. Following cleaning, the aerosol-nucleation chamber is filled with pure nitrogen (N_2). Next, we pass pure N_2 through a bubbler filled with ultrapure water from a Milli-Q, creating a mixture of water vapor and droplets suspended in the N_2 carrier gas. The bubbler is equipped with an electrically heated, feedback-controlled thermal jacket capable of reaching 100 °C, although this system was not used in the present experiments. The bubbler can also be used to produce vapors other than water, but only water vapor is used in the present experiments. The resulting water/N_2 mixture passes through a two-stage compressed gas filter to remove any droplets or particles with diameters above $d > 5$ μm, resulting in a stream of humid air. This humid air is injected into the aerosol-nucleation chamber at a flow rate of 10 standard liters per minute (SLPM) using a mass flow controller (Alicat Scientific) until the desired S_0 is reached.

Next, we set the concentration of dry seeding aerosol particles, C_0, in the aerosol-nucleation chamber. Aerosols are injected using a two-stage powder dispersion system, similar to those described by Sullivan *et al.*[40] and Huynh and McNeill.[41] A schematic of the aerosol injection system is shown in the top left of Fig. 1(a). The system consists of two 2 L Erlenmeyer flasks connected in series with the first flask connected to an N_2 source and the second to the aerosol-nucleation chamber. Aerosol powder of known composition is placed in the first flask along with a Teflon-coated stir bar. The flask is placed on a stir plate set to continuously stir the powder. A mass flow controller (Alicat Scientific) is used to inject dry N_2 into the first flask at a flow rate of 0.4 to 5 SLPM. The N_2 entrains aerosol particles from the first flask in the flow, then passes into the second flask, and eventually passes into the aerosol-nucleation chamber. Sharp turns are introduced into the tubing and inside the second flask to trap large particles, thereby enhancing the selection of small particles. During the initial preparation of the aerosol-nucleation chamber, the fans mounted inside the chamber are kept on to assist with the mixing of humid air and seeding particles.

For all experiments described in this paper, the aerosol-nucleation chamber is seeded with calcium carbonate particles ($CaCO_3$, 99% pure, American Elements Inc., nominal size of 100 nm). We choose $CaCO_3$ to demonstrate the capabilities and simple usage of the chamber and associated instrumentation. In future experiments, other seeding aerosols relevant to cloud microphysics (e.g., mineral dust, sea salt, and soot) will be explored to assess the role of hygroscopicity in cloud droplet nucleation.[42]

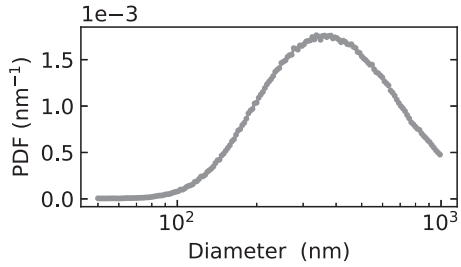

FIG. 2. Probability density function (PDF) of the diameter distribution of solid calcium carbonate ($CaCO_3$) aerosol particles introduced into the aerosol-nucleation chamber measured using a scanning mobility particle sizer.

C. Aerosol measurements

Two separate measurement systems are used to characterize the seeding aerosols. We use a scanning mobility particle sizer (SMPS) to record size distributions and a condensation particle counter (CPC) to record concentrations.

The SMPS (TSI) is used to characterize the diameter distribution of the dry $CaCO_3$ particles injected into the chamber, measuring particle sizes between 10 nm and 1 μm. Our SMPS configuration includes an advanced aerosol neutralizer (TSI model 3088), an electrostatic classifier (TSI model 3082), a differential mobility analyzer (TSI model 3081), and a condensation particle counter (TSI model 3752). Figure 2 shows the probability density function (PDF) of the $CaCO_3$ particle diameter as measured with the SMPS. This distribution is centered around $\bar{d}$ = 316 nm with a standard deviation of 257 nm. The difference between the nominal 100 nm particle diameters and the measured diameters is likely due to the coagulation of the aerosols during their preparation and seeding. The PDF is insensitive to the N_2 flow rate used in the powder dispersion system.

We use a separate CPC (TSI model 3007) to measure the concentrations of aerosols up to 10^5 #/cm^3 with an accuracy of ±20%. The CPC is sensitive to particles larger than 10 nm in diameter. We use the CPC to sample air from the aerosol-nucleation chamber during the preparation of the experiment to confirm that room aerosols inside the aerosol-nucleation chamber are removed down to a base concentration of 1–2 #/cm^3. We also use the CPC to record the $CaCO_3$ concentration after chamber initialization, just prior to triggering an expansion.

D. Droplet measurements

We characterize the droplets that appear during an expansion using a phase Doppler anemometry (PDA) system (a Dantec Inc. flow explorer, a HiDense FiberPDA optical receiver, and a burst spectrum analyzer). In its present configuration, our PDA system can record droplet diameter distributions between 1 and 50 μm as well as horizontal and vertical droplet velocity distribu-

09 May 2025 20:58:15

© Author(s) 2025

tions. The flow explorer consists of two lasers with wavelengths of 532 and 561 nm. Each beam is split into two; the resulting four beams intersect at a measurement region of ~0.013 mm^3 in volume and with a projected area of $A = 0.119 \times 0.1196$ mm^2. The measurement volume is located close to the center of the aerosol-nucleation chamber, ~26.7 cm from the bottom of the chamber and 15.5 cm from the walls. Horizontal and vertical droplet speeds as well as diameters are recorded for all droplets that pass through the measurement volume with a sampling rate of up to 1 MHz. Detected droplets with diameters smaller than 1 μm are removed from the dataset as they are below the measurement accuracy threshold.

In addition, we use cinematic inline holography to measure droplet statistics, including size, number, concentration, and speed. A detailed description of this system is provided by Erinin *et al.*[36] We use this technique in Sec. III D to report on the temporal evolution of droplet diameters and concentration during an expansion. In these experiments, the system is recording at a frame rate of 600 Hz and has a spatial resolution of 1.41 μm with an ability to measure droplets with diameters down to about 6 μm.

The PDA system is designed to operate in relatively dense spray and provides statistics at a single point in space. In contrast, holography probes droplet concentration, size, and speed over an extended path length and operates at low droplet concentrations. Holography is especially suited to measurements of ice particles,[43] which often nucleate in low concentrations and form nonspherical shapes. In the present paper, we use PDA for experiments with large pressure drops and seeding aerosol concentrations from 10^2 to 10^5 #/cm^3, yielding droplet concentrations of similar orders of magnitude. We use holography for experiments with lower aerosol concentrations (1–100 #/cm^3) carried out closer to the onset of droplet nucleation. Note that PDA has a much smaller measurement volume than the holography system. Holography can, therefore, record a larger number of individual droplets than PDA despite operating in a less dense cloud.

III. RESULTS AND DISCUSSION

We now present the characterization of the REACh facility in terms of thermodynamic conditions and flow and then demonstrate its capabilities to analyze droplet heterogeneous nucleation for a range of initial aerosol concentration and saturation conditions. Table I details the experimental conditions for all results presented in this paper.

In Secs. III A and III B, we characterize the thermodynamic and flow conditions during expansion experiments for a range of pressure drops and initial saturation ratios, with both forced and unforced mixing. We compare the minimum temperature reached during each expansion to dry and moist adiabatic theories.

In Secs. III C and III D, we present an analysis of conditions where droplets are formed in the presence of seeding $CaCO_3$ aerosols, for various initial saturation ratios, aerosol concentrations, and mixing conditions. We leverage both PDA (Sec. III C) and holography (Sec. III D) to probe high and low ranges of aerosol and droplet concentration, respectively. In Sec. III C, we present PDA data from experiments over a range of S_0 conditions, sweeping the concentration of seeding $CaCO_3$ particles from 100 to 10^5 #/cm^3. The same datasets are collected for both unforced and forced mixing conditions. For all experiments in Sec. III C, the initial temperature and pressure are 20 °C and 1 bar, respectively, and the pressure drop is always $\Delta p = 0.54$ bar. In Sec. III D, we demonstrate the use of holography to track time-resolve droplet growth. This experiment is performed for a small seeding aerosol concentration, and we consider a lower pressure drop ($\Delta p = 0.36$ bar) relatively close to the onset of droplet heterogeneous nucleation.

A. Thermodynamics during the expansion

Here, we describe the measurements of thermodynamic properties inside the chamber throughout an expansion and compare these results with theoretical predictions. Figure 3 shows the chang-

09 May 2025 20:58:15

TABLE I. Summary of experimental conditions. Thermodynamic measurements are used to characterize the chamber (Secs. III A and III B). Droplet statistics measurements are collected with PDA for experiments with high aerosol concentrations (Sec. III C), while experiments with low aerosol concentrations targeting droplet growth near the onset of nucleation are performed with holography (Sec. III D). The initial saturation ratio, S_0, and initial $CaCO_3$ aerosol concentration, C_0, are provided for each dataset along with mixing conditions. Note that $C_0 \leq 0.0002$ corresponds to a clean chamber scoured of particles within the detection limit of the CPC.

Dataset	Mixing	S_0	Δ P (bar)	$C_0 \times 10^4$ (#/cm^3)	No. of runs	Figure no.
Thermodynamic	Unforced	0	0–0.54	≤0.0002	11	4
Thermodynamic	Unforced	0.5	0–0.54	0.2	11	4
Thermodynamic	Unforced	0.3	0.54	0.175–7.05	8	5
Droplet statistics (PDA)	Unforced	0.3	0.54	0.174–24.77	7	11 and 12
Droplet statistics (PDA)	Unforced	0.5	0.54	0.141–6.37	8	11 and 12
Droplet statistics (PDA)	Unforced	0.7	0.54	0.174–6.49	8	6 and 8–11
Droplet statistics (PDA)	Forced	0.3	0.54	0.190–5.03	8	11
Droplet statistics (PDA)	Forced	0.5	0.54	0.165–5.74	7	11
Droplet statistics (PDA)	Forced	0.7	0.54	0.169–6.78	7	6 and 8–10
Droplet statistics (PDA)	Forced/unforced	0.7	0.54	18.5	1	3 and 7
Droplet growth (holography)	Unforced	0.3	0.36	0.007	1	12

© Author(s) 2025

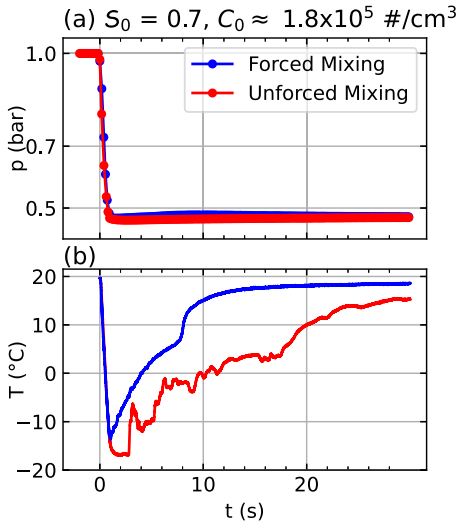

FIG. 3. Time series of (a) pressure and (b) temperature measured during an expansion with Δp = 0.54 bar, S_0 = 0.7, and $C_0 = 1.8 \times 10^5$ #/cm^3. Both unforced mixing (red) and forced mixing (blue) cases are shown. The pressure drop is complete in <1 s in both mixing cases. No measurable differences are observed in the initial temperature decrease (t < 0.5 s); however, there is a 3 °C difference in the minimum temperature, T_{min}, reached between the two cases. Shortly after T_{min} is reached, the chamber begins to thermally equilibrate with the room. This thermalization process is faster in the forced mixing case as the fans induce turbulent mixing.

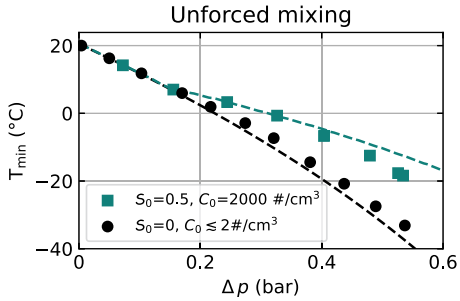

FIG. 4. Minimum temperature reached during each expansion as a function of the pressure drop Δp. Data are shown with unforced mixing for dry conditions (S_0 = 0) with minimal seeding aerosol particles (black circles) and moist (S_0 = 0.5) conditions with C_0 = 2000 #/cm^3 (teal squares). The markers correspond to the experimental data, while the dashed curves are given by Eq. (1) in the dry case and Eq. (10) in the moist case.

ing pressure and temperature during an expansion with an initial saturation ratio of S_0 = 0.7 and an initial $CaCO_3$ particle concentration of $C_0 = 1.8 \times 10^5$ #/cm^3. Such large particle concentrations, while not typical of the atmosphere, allow condensation to keep up with supersaturation generation during experiments with large pressure drops, keeping the supersaturation ratio close to unity. As described in Sec. II A, fans are installed inside the chamber to enhance the mixing of humid air and aerosols and can be left on during an expansion. We show results for experimental runs with both fans off (unforced mixing, red curves) and fans on (forced mixing, blue curves).

In both the unforced and forced mixing cases, the rapid pressure decrease lasts ~1 s [Fig. 3(a)] and is accompanied by a decrease in temperature [Fig. 3(b)]. In all experiments, the initial temperature is that of the room, 20 °C. Shortly after the expansion, the temperature reaches a minimum and then subsequently increases as the air returns to thermal equilibrium via heat conduction through the chamber walls. In the unforced mixing case, the minimum temperature reached in the center of the chamber is 3 °C colder than in the forced mixing case and persists for ~3 s. The air then thermalizes over the following ~30 s fluctuating by ±5 °C, likely due to large-scale convective air currents inside the chamber. By contrast, this thermalization process lasts only ~15 s in the forced mixing case as the fans enhance the thermal conduction of heat through the air–wall boundary.

In both experiments shown in Fig. 3, a sudden temperature increase is observed during the thermalization process, occurring ~17 s after the expansion is triggered in the unforced mixing case and after ~6 s in the forced mixing case. These times correspond approximately to the cloud lifetime, τ_f, which we define as the length of time over which cloud droplets are present and detectable after an expansion. Measurements of the cloud lifetime are discussed in more detail in Sec. III C 2. Eventually, the cloud of droplets evaporates; thermalization can then accelerate afterward, as the heat flux from the chamber walls goes entirely toward sensible heating (raising the temperature), rather than providing latent heat for droplet evaporation. This process explains the sudden changes observed in temperature as the chamber returns to thermal equilibrium.

The minimum temperature reached in the aerosol-nucleation chamber during an expansion, T_{min}, is a key thermodynamic variable and is an important determining factor for the total condensed water in an expansion. In Fig. 4, we report T_{min} for a series of pressure drops with $\Delta p = p_f - p_0$ ranging from 0.02 to 0.54 bar. Figure 4 shows results for both the dry expansion case with S_0 = 0 and minimal seeding aerosols and the moist expansion case with S_0 = 0.5 and C_0 = 2000 #/cm^3. In both cases, T_{min} decreases as Δp increases.

The dry (S_0 = 0) experiments can be modeled as a dry adiabatic expansion, with[44]

$$T_f = T_0 \left(\frac{p_f}{p_0} \right)^{\frac{\gamma-1}{\gamma}}, \tag{1}$$

where T_0 and p_0 are the initial temperature and pressure, respectively; T_f and p_f are the final temperature and pressure, respectively, after the expansion is complete; and $\gamma = C_p/C_V$ is the ratio of specific heats for dry nitrogen. T_f can be directly replaced by T_{min}. The black dashed line in Fig. 4 shows T_{min} given by Eq. (1) with the measured values of p_0, T_0, and p_f and γ = 1.4. This calculation shows good agreement with the experimentally measured T_{min}.

The maximum possible saturation ratio S_{max} reached during an expansion can be estimated from the pressure drop and the dry adiabatic minimum temperature according to $S_{max} = e/e^*(T_{min})$. Assuming an adiabatic expansion,[17] the water vapor pressure is estimated as $e = e_0 \times (p_f/p_0)$, where e_0 is the initial water vapor pressure set by S_0, p_0 is the initial total chamber pressure, and p_f is

09 May 2025 20:58:15

© Author(s) 2025

the final chamber pressure after expansion. Assuming $S_0 = 0.3$, for the highest pressure drop $\Delta p = 0.54$ bar, we obtain S_{max} values as high as 10, while $\Delta p = 0.42$ bar yields $S_{max} \approx 4$ and $\Delta p = 0.23$ bar yields $S_{max} \approx 1$. We note that the highest S_{max} values are not actually reached in the chamber as water vapor is lost through condensation on seeding aerosols. We rather indicate that the available pressure drops create conditions highly conducive to droplet nucleation and growth.

Most of our expansion experiments are carried out in a humid environment, where Eq. (1) is no longer valid. In order to validate the thermodynamics of moist expansions, we must modify to Eq. (1) to account for humidity. Determining T_f as a function of p_f for humid air with $0 < S_0 < 1$ requires two ingredients. First, we must determine the temperature T_{sat} and pressure p_{sat} at which the expanding humid chamber air initially reaches saturation ($S = 1$), and second, we must generalize Eq. (1) for saturated air.

We begin by noting the following relations where again e denotes the partial pressure of water vapor and $e^*(T)$ is the partial pressure of water vapor at saturation for temperature T:

$$\left(\frac{T_{sat}}{T_0}\right)^{C_p/R_d} = \frac{p_{sat}}{p_0} \tag{2}$$

$$= \frac{e_{sat}}{e_0} \tag{3}$$

$$= \frac{e^*(T_{sat})}{S_0\, e^*(T_0)} \tag{4}$$

$$= \frac{1}{S_0} \exp\left[-\frac{L_v}{R_v}\left(\frac{1}{T_{sat}} - \frac{1}{T_0}\right)\right]. \tag{5}$$

The first equality in the above expressions follows from Eq. (1); the second follows from the fact that the partial pressure of water vapor scales with the total pressure in the absence of condensation; the third arises from the definitions $e_{sat} = e^*(T_{sat})$ and $S_0 = e_0/e^*(T_0)$; and the last derives from the Clausius–Clapeyron relationship for $e^*(T)$, namely $de^*/dT = -(L_v/R_v T^2)e^*(T)$.[44] Note that R_d and R_v are the gas constants for N_2 and water vapor, respectively, and L_v is the latent heat. Here, we take L_v to be a constant, as accounting for its variation with temperature throughout an expansion modifies the calculations of the minimum temperature in the chamber by less than 2%.

Similar to the manipulations performed by Romps,[45] we solve the above equation for T_{sat} in terms of S_0 using the "−1" branch of the Lambert W-function, which satisfies $W(xe^x) = x$, obtaining

$$T_{sat} = \frac{-c_i}{W_{-1}\left(-S_0^{R_d/C_p} c_i e^{-c_i}\right)} T_0, \tag{6}$$

where $c_i \equiv R_d L_v/(C_p R_v T_0)$. Equation (6) can then be combined with Eq. (2) to obtain an equation for p_{sat},

$$p_{sat} = p_0 \left[\frac{-c_i}{W_{-1}\left(-S_0^{R_d/C_p}\, c_i\, e^{-c_i}\right)}\right]^{C_p/R_d}. \tag{7}$$

Note that with T_{sat} and p_{sat} determined, we can now determine the specific humidity q_{sat} (kg H_2O/kg humid air) at the point of first saturation in terms of the saturation specific humidity q^* evaluated at (T_{sat}, p_{sat}),

$$q_{sat} = q^*(T_{sat}, p_{sat}) = \frac{R_d}{R_v}\frac{e^*(T_{sat})}{p_{sat}}. \tag{8}$$

We note that because S might exceed 1 in the chamber, T_{sat} will be an upper bound of the minimal temperature, while T_{min} obtained from the dry adiabat will be a lower bound.

With T_{sat}, p_{sat}, and q_{sat} in hand, we now seek a relation between T and p after the parcel saturates, assuming that condensation occurs sufficiently rapidly to keep S close to 1 [i.e., $S - 1 \sim \mathcal{O}(0.01)$] throughout the process. This requires accounting for the effects of the latent heat of condensation on the parcel as it expands and cools. To proceed analytically, we utilize the formula for $q^*(T)$ along such a parcel trajectory as derived by Romps.[46] This formula, unlike the more general formula Eq. (8), gives q^* as a function of T along a moist adiabat with initial temperature T_{sat} and initial specific humidity q_{sat}, where the p-dependence of q^* appearing in Eq. (8) is implicitly accounted for using moist adiabatic thermodynamics. The result is somewhat involved but can again be expressed analytically in terms of the Lambert W-function,

$$q^*(T) = \frac{R_d T_0}{L_v} W_0\left(y_{sat}\, e^{-f(T_{sat}-T)}\right), \tag{9}$$

$$\text{where} \quad y_{sat} \equiv \frac{L_v q^*(T_{sat})}{R_d T_0} \exp\left(\frac{L_v q^*(T_{sat})}{R_d T_0}\right)$$

$$\text{and} \quad f \equiv \frac{L_v}{R_v T_0^2} - \frac{C_p}{R_d T_0}.$$

Evaluating Eq. (9) at the final temperature T_f and combining it with Eq. (8) allow us to solve for the final pressure p_f in terms of the final temperature T_f,

$$p_f = \frac{R_d}{R_v}\frac{e^*(T_f)}{q^*(T_f)}. \tag{10}$$

This yields the desired relationship between the final (minimum) temperature T_f and the pressure drop $\Delta p = p_0 - p_f$.

Figure 4 shows the comparison of the measured values of T_{min} with those predicted by Eq. (10) for a representative humid expansion (teal trace and markers). We observe a good agreement between data and theory for pressure drops up to $\Delta p = 0.45$ bar.

T_{min} calculated from the dry adiabatic expansion is the lower temperature limit if no condensation occurs. Since the process of condensation releases energy, we expect the temperature to remain above that bound. Our thermodynamic model for drop formation assumes that $S \lesssim 1$ (i.e., enough vapor condenses to maintain equilibrium), but in instances where $S > 1$, the temperature will be lower than what is predicted by Eq. (10). We, therefore, consider the dry adiabat as a conservative uncertainty estimate of the lowest possible temperature.

Finally, we characterize how the expansion thermodynamics are impacted by the presence of various concentrations of seeding aerosols. Figure 5 shows the time evolution of temperature during

09 May 2025 20:58:15

© Author(s) 2025

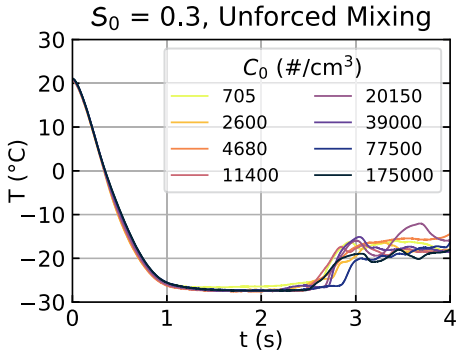

FIG. 5. Temperature time series during expansions for different initial aerosol concentrations, C_0, performed with unforced mixing, an initial saturation ratio of $S_0 = 0.3$, and a pressure drop of $\Delta p = 0.54$ bar. The expansion is triggered at $t = 0$ s. No notable dependence of the temperature curves on C_0 is observed during the expansion, from $t = 0$ to 2.5 s. For $t > 2.5$ s, differences in the temperature response are likely due to post-expansion air mixing.

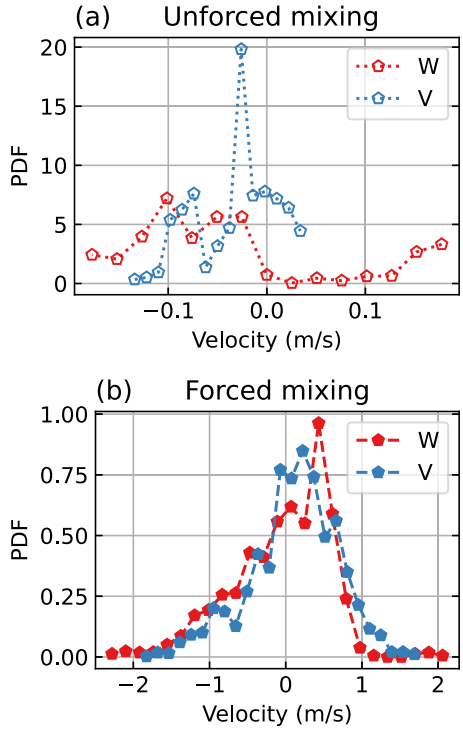

FIG. 6. Probability density functions (PDFs) of droplet velocities recorded with phase Doppler anemometry (PDA) during expansions with (a) unforced mixing conditions (dotted lines) and (b) forced mixing conditions (dashed lines). V (blue) corresponds to the horizontal component of the velocity field, and W (red) corresponds to the upward vertical component in the plane orthogonal to the PDA laser beams; see Fig. 1 for a graphical orientation of the axes. Experiments are conducted with $S_0 = 0.7$, $C_0 = 8 \cdot 10^4$ #/cm^3, and $\Delta p = 0.54$ bar.

expansions with different aerosol concentrations, C_0. These experiments are carried out with unforced mixing, an initial saturation ratio of $S_0 = 0.3$, and the maximum pressure drop of $\Delta p = 0.54$ bar. The dependence of $T_{\min}$ on C_0 is found to be very weak, with variations of at most 0.5 °C. After the expansion, for times $t > 2.5$ s, random temperature fluctuations are observed, which vary from run to run. We note that this insensitivity of $T_{\min}$ to C_0 is likely due to the relatively large aerosol concentrations used here, which keep S close to 1 despite the large pressure drop.

B. Flow under forced and unforced mixing conditions

We now characterize mixing inside the aerosol-nucleation chamber by comparing droplet velocity statistics acquired with phase Doppler anemometry for unforced and forced mixing conditions. Velocity distributions and statistics are collected over the full time of the expansion experiment.

Figure 6 shows representative horizontal (V) and vertical (W) velocity PDFs for both mixing cases with $S_0 = 0.7$ and $C_0 = 8 \times 10^4$ #/cm^3. In the unforced mixing case [Fig. 6(a)], the droplets feature horizontal and vertical velocity distributions that are not centered about zero and do not have clearly defined shapes due to the limited statistics. In the forced mixing case [Fig. 6(b)], a random turbulent flow is induced by the motion of the fans. Both V and W have peaks at ~0.2 m/s. The V and W distributions display absolute values nearly an order of magnitude larger in the forced mixing case than in the unforced mixing case. Velocity distributions are similar across various C_0, S_0, and Δp conditions tested.

We define the mean droplet speed as $\tilde{U} = \overline{\sqrt{V^2 + W^2}}$, where V and W are the measured velocities by PDA and the overline indicates the average over drops passing through the sensor over time. We define a characteristic fluctuating velocity as $\mathscr{U} = \sqrt{\sigma_V^2 + \sigma_W^2}$, where σ represents the standard deviation. The mean droplet speed under forced mixing is $\tilde{U}_{\text{forced}} = 0.8$ m/s and under unforced mixing is $\tilde{U}_{\text{unforced}} = 0.1$ m/s, with variations of less than 0.1 and 0.01 m/s across conditions, respectively. The characteristic velocity fluctuations ($\mathscr{U}$) are very similar than the means so that either can be used as characteristic velocity in the rest of this paper.

The mixing in the chamber can be dominated either by diffusion or by turbulent mixing; this distinction is characterized by the Péclet number, $\mathscr{P}_e$. $\mathscr{P}_e$ is defined as the ratio of the diffusion timescale, $\tau^{\text{diff}} = L^2/\alpha$, divided by the advective turbulent mixing timescale, $\tau^{\text{adv}} = L/\tilde{U}$, where L and $\tilde{U}$ represent the characteristic length-scale and speed of the flow and α represents the thermal diffusivity of the gas inside the chamber. We can, therefore, express the Péclet number as

$$\mathscr{P}_e = \frac{\tau^{\text{diff}}}{\tau^{\text{adv}}} = \frac{L\tilde{U}}{\alpha}. \tag{11}$$

Taking $L = 0.5$ m, $\alpha = 1.9 \times 10^{-5}$ m^2/s at 0 °C, and $\tilde{U}$ as the experimentally measured average droplet speed, the order of magnitude of the Péclet numbers for the unforced and forced mixing cases is $\mathscr{P}_{e,\text{unforced}} = 2.7 \times 10^3$ and $\mathscr{P}_{e,\text{forced}} = 2.2 \times 10^4$, respectively. Both cases feature $\mathscr{P}_e \gg 1$ and are, therefore, dominated by turbulent mixing. The difference in the mixing timescales between the two cases can be estimated by

09 May 2025 20:58:15

© Author(s) 2025

$$\frac{\tau^{\text{adv}}_{\text{unforced}}}{\tau^{\text{adv}}_{\text{forced}}} = \frac{\bar{U}_{\text{forced}}}{\bar{U}_{\text{unforced}}} \approx 8. \tag{12}$$

Mixing is about eight times faster in the forced mixing case, confirming that the fans will enhance the chamber thermalization after an expansion.

C. Droplet nucleation as a function of seeded aerosols, saturation, and mixing

We now characterize droplet heterogeneous nucleation as a function of initial aerosol concentration and saturation ratio. We perform a parameter sweep over 46 conditions while tracking the size and number of droplets formed throughout the expansion. All experiments described herein are performed at the maximum pressure drop (Δp = 0.54 bar).

1. Droplet nucleation and growth

We start by discussing the droplet nucleation and subsequent growth for a typical expansion experiment. Figure 7 shows the time evolution of the thermodynamic chamber parameters alongside droplet statistics measured with PDA from the time the pressure drop is initiated (t = 0 s) to the point where most droplets have disappeared ($t \approx 8$ s). These data are from a single representative expansion with S_0 = 0.7 and $C_0 = 1.8 \times 10^5$ #/cm^3 under forced mixing conditions. As discussed in Sec. III A, the sharp drop in pressure [Fig. 7(a)] triggers a rapid temperature decrease [Fig. 7(b)]. The drop in temperature causes a sudden increase in saturation ratio, which initiates the nucleation of water droplets.

Figure 7(c) plots the time evolution of N, the number of droplets detected per 0.17 s time interval, beginning shortly after the expansion occurs. N increases until time τ_m, as marked with black vertical lines in Figs. 7(c)–7(f). The cloud lifetime, τ_f, is the point after which very few droplets are detected as marked with a red vertical bar in Figs. 7(c)–7(f).

The temporal evolution of the mean droplet speed, $\bar{U}$ (see Sec. III B), is shown Fig. 7(d). Over the time window $0 < t < \tau_m$, the mean droplet speed is found to increase from ~0.2 to 1.1 m/s. The increase in velocity is related to the large-scale flow that occurs in the chamber during the expansion. For $t > \tau_m$, this increased mean droplet speed is sustained for several seconds after which it decreases as t approaches τ_f and the cloud dissipates.

The time evolution of the mean droplet diameter, $\bar{d}$, is shown in Fig. 7(e). During the initial stages of droplet growth, $\bar{d}$ increases from ~1 μm at t = 0 s to ~4 μm at t = 0.5 s and then stays nearly constant until t approaches τ_f.

The swarm plot in Fig. 7(f) illustrates each detected droplet as a point. This plot captures the evolution of both the droplet number in the vertical width of the swarm and the droplet diameter, as indicated by the color of each point. After $t > \tau_f$, most droplets have evaporated.

A notable feature of the data shown in Fig. 7 is that the droplet diameter $\bar{d}$ is fairly constant between τ_m and τ_f, while droplets are evaporating and N is decreasing. This is consistent with the "inhomogeneous mixing" paradigm,[47,48] where the time it takes for thermodynamic cloud properties (such as temperature) to homogenize is much longer than the time it takes for droplets to equilibrate with their local environment. In this paradigm, heat transferred from the chamber walls completely evaporates the droplets only in nearby pockets of air, rather than rapidly mixing throughout the volume and partially evaporating droplets throughout. This leads to little change in $\bar{d}$ but a change in the average N passing through the PDA detection volume. These results support recent reports, suggesting that inhomogeneous mixing is a rather ubiquitous phenomenon in cloudy air masses.[7,37,49]

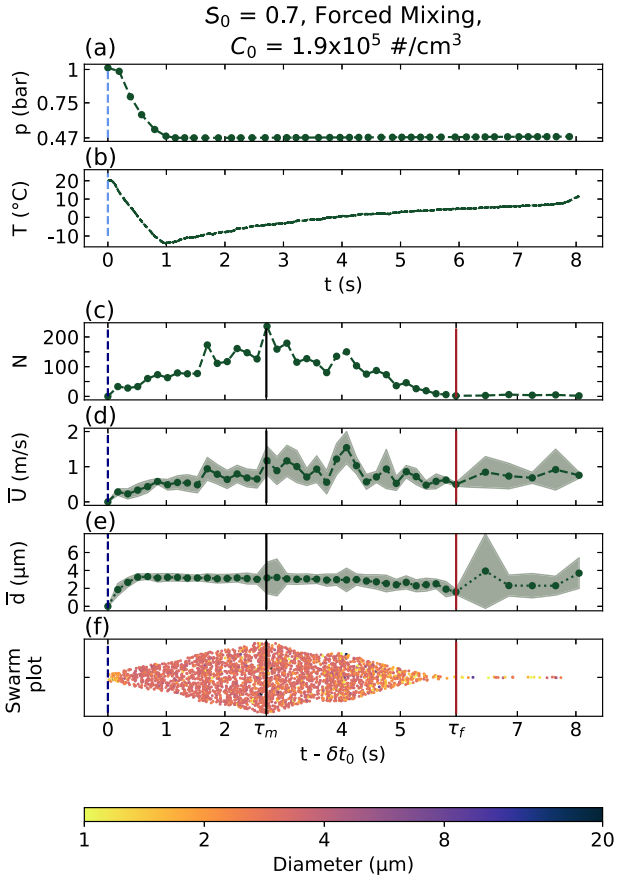

FIG. 7. Time series of (a) pressure, (b) temperature, (c) number of droplets detected per 0.17 s time interval, N, (d) running mean droplet speed $\bar{U} = \overline{\sqrt{V^2 + W^2}}$, (e) running mean droplet diameter, $\bar{d}$, and (f) a swarm plot of individual droplet sizes. Panels (c)–(f) show data collected with PDA. All data are collected in real time for a single expansion with Δp = 0.54 bar and forced mixing. The initial conditions are S_0 = 0.7 and $C_0 = 1.9 \times 10^5$ #/cm^3. $\bar{U}$ and $\bar{d}$ are calculated over a time interval of 0.17 s, and the green contours around their curves represent ±1 standard deviation. The swarm plot in panel (f) provides a compact representation of the droplet number and size shown in panels (c) and (e); each point represents one detected droplet. The evolution of the number of particles is captured by the thickness of the swarm plot on the vertical axis. The color of each point represents the diameter of that droplet according to the color bar at the bottom of the figure. The light blue dashed vertical line in panels (a) and (b) represents the moment the valve opens and the expansion begins. The black dashed vertical line in panels (c)–(f) marks the time at which the first droplet is detected. The exact time difference between these two events, δt_0, is on the order of ~0.7 s. τ_m and τ_f denote the middle and end of the cloud lifetime, respectively, and are indicated by the black and red solid vertical lines in panels (c)–(f).

09 May 2025 20:58:15

© Author(s) 2025

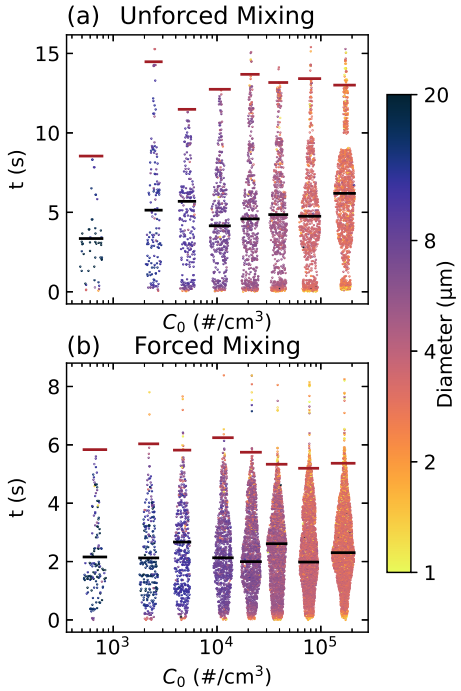

FIG. 8. Swarm plots summarizing the time evolution of droplet number and diameter while sweeping initial aerosol concentration, C_0, for (a) unforced and (b) forced mixing with $S_0 = 0.7$ and $\Delta p = 0.54$ bar. The swarm plots use PDA data to show droplet counts, indicated by dots, and diameter, indicated by dot colors. The black and red horizontal bars represent τ_m and τ_f, respectively. Droplets colored in yellow have measured diameters between $d = 0.1$ and 1 μm.

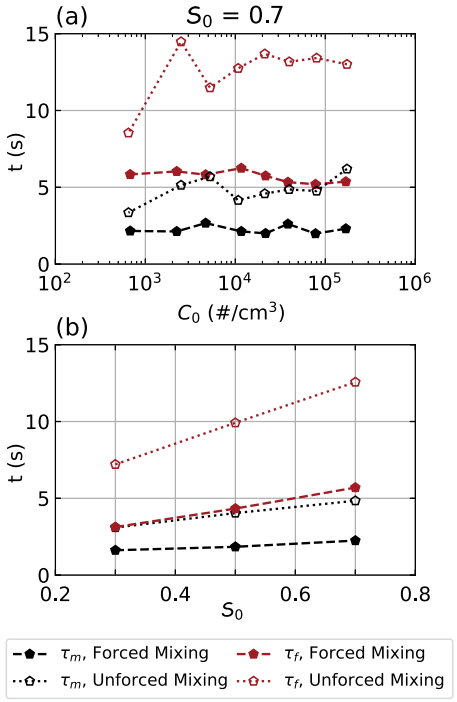

FIG. 9. Characteristic timescales of the droplet cloud, τ_m (black points) and τ_f (red points), as a function of (a) initial aerosol concentration, C_0, and (b) saturation ratio, S_0. Data are shown for both unforced mixing (empty markers) and forced mixing (solid markers). In panel (a), $S_0 = 0.7$, while C_0 is swept. The timescales plotted in panel (b) are calculated by averaging data collected over all values of C_0 for each value of S_0.

2. Cloud lifetime

We now examine the cloud lifetime, τ_f, as a function of the initial saturation ratio, initial aerosol concentration, and mixing conditions. Figure 8 shows several swarm plots illustrating the time-dependent number and size distribution of droplets for various initial aerosol concentrations, C_0. For the smaller values of C_0 tested, characterization becomes challenging as very few droplets are measured. An initial saturation ratio of $S_0 = 0.7$ is used for all experiments reported in Fig. 8.

In the unforced mixing cases shown in Fig. 8(a), the droplet number gradually grows to a maximum around $\tau_m = 5$–6 s, as marked with black horizontal bars, and decays to nearly zero by $\tau_f = 10$–15 s, as marked with red horizontal bars. In the forced mixing cases in Fig. 8(b), the peak droplet numbers are instead reached at $\tau_m = 2$–3 s, while droplets disappear by $\tau_f = 6$ s. The droplet cloud lives less than half as long under forced mixing as under unforced mixing; again, the fans speed the thermalization process. As in Fig. 7, droplet diameters are observed to be fairly constant in time, while the droplet number decreases between τ_m and τ_f, again indicative of inhomogeneous mixing.

Figure 9(a) shows the extracted τ_m and τ_f timescales as a function of C_0 from the same experimental datasets reported in Fig. 8. τ_m and τ_f appear to be independent of C_0. The only notable trend is that all timescales are shorter with forced mixing, as we have already noted. Meanwhile, Fig. 9(b) shows τ_m and τ_f as a function of S_0. Both τ_m and τ_f increase as S_0 increases. As we will see in Sec. III C 3, a higher initial water content facilitates the growth of droplets to larger average diameters, which then persist for a longer period of time before evaporating.

3. Scaling of droplet statistics

We now analyze the total number of nucleated droplets and their mean sizes as functions of initial aerosol concentration and saturation ratio. We explored calculating the total number of droplets by integrating N over either $0 < t < \tau_m$ or $0 < t < \tau_f$. Both methods give similar trends as functions of C_0 and S_0. The mean droplet diameter $\overline{d}$ is also nearly identical when evaluated over both time windows. We, therefore, define N_{tot} as the total number of droplets detected by PDA over $0 < t < \tau_f$ and $\overline{d}$ as the mean droplet diameter averaged over the same window as counting more droplets yields better statistics.

Figure 10(a) shows the dependence of the total droplet number, N_{tot}, on C_0 and S_0 for both unforced and forced mixing. As C_0 increases, N_{tot} increases; this trend remains consistent across all S_0 and mixing conditions. N_{tot} is also observed to increase with S_0. The relationship between N_{tot} and S_0 is related to the longer droplet cloud lifetime [see Fig. 9(b)].

09 May 2025 20:58:15

© Author(s) 2025

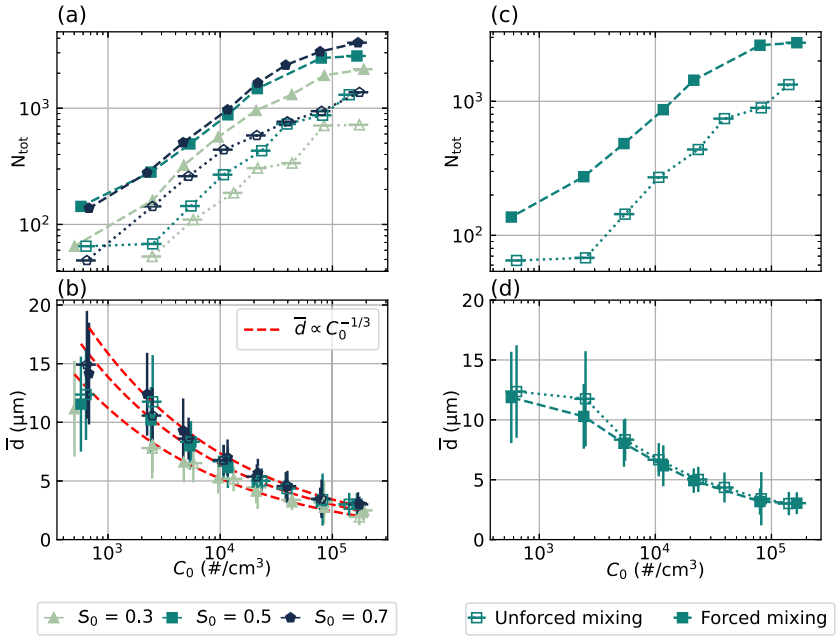

FIG. 10. Droplet statistics as a function of initial aerosol concentration, saturation ratio, and mixing conditions. (a) The total number of droplets detected, N_{tot}, and (b) their mean diameter, $\bar{d}$, as a function of C_0 for S_0 = 0.3, 0.5, and 0.7 and both unforced and forced mixing. (c) N_{tot} and (d) $\bar{d}$ plotted as a function of C_0 for S_0 = 0.5. The vertical error bars show ±1 standard deviation in measurement error, and the horizontal error bars show measurement uncertainty in C_0. Data for S_0 = 0.3, 0.5, and 0.7 are plotted with triangle, square, and pentagon markers, respectively, while unforced and forced mixing cases are plotted with empty and filled markers, respectively. The red dashed lines show the $\bar{d} \propto C_0^{-1/3}$ power-law scaling given in Eq. (15).

Figure 10(b) plots the dependence of the mean droplet diameter, $\bar{d}$, on C_0 and S_0 for both unforced and forced mixing. $\bar{d}$ consistently decreases with increasing C_0 and increases with increasing S_0.

Figures 10(c) and 10(d) highlight how N_{tot} and $\bar{d}$ compare between unforced and forced mixing for S_0 = 0.5. $\bar{d}$ is not significantly affected by the mixing conditions for any value of C_0. Meanwhile, N_{tot}, which quantifies the number of droplets that pass through the measurement plane, is consistently larger under forced conditions than under unforced conditions. This can be attributed to the difference in characteristic mixing velocity—either the mean droplet speed $\tilde{U}$ or the fluctuating velocity $\mathscr{U}$, see Sec. III B—between the two mixing conditions. The dependence of N_{tot} on mixing is, therefore, due to enhanced flow in the forced mixing case, which causes more particles to pass through the measurement volume per unit time. In fact, when N_{tot} is normalized by $\tilde{U}$, the data collected under forced and unforced conditions collapse; see Fig. 11.

To further analyze the various trends observed in Fig. 10, we now introduce a scaling analysis to understand the fraction of water vapor that is transformed into liquid and rationalize the size and number of droplets formed in each experiment. First, we must relate N_{tot}, the total number of droplets that pass through the PDA measurement region, to an absolute droplet concentration C_{drop} in units of #/cm^3. We define C_{drop} as

$$C_{drop} = \frac{N_{tot}}{A\,\mathscr{U}_{rms}\,\tau_f}, \tag{13}$$

where A is the area of the measurement plane, $\mathscr{U}_{rms}$ is the characteristic speed of droplets passing through the measurement plane, and τ_f is the cloud lifetime. The area of the measurement region is known from the calibration of the PDA system, A = 0.119 × 0.1196 mm^2; see Sec. II D. The definition of C_{drop} naturally encapsulates the importance of S_0 and the mixing (flow) conditions through its dependence on τ_f and $\mathscr{U}_{rms}$.

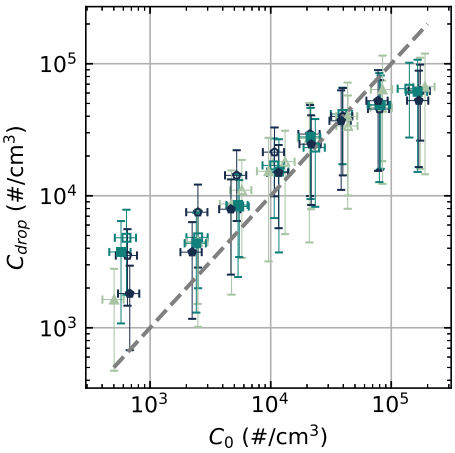

FIG. 11. Droplet concentration, C_{drop}, as a function of initial aerosol concentration, C_0, for all experimental conditions. Data for S_0 = 0.3, 0.5, and 0.7 are plotted with triangle, square, and pentagon markers, respectively, while unforced and forced mixing cases are plotted with empty and filled markers, respectively. C_{drop} is calculated using Eq. (13). The gray dashed line has a slope of C_{drop}/C_0 = 1.

Prior to an expansion, the water vapor concentration is set by S_0, which determines the mass of liquid vapor available for condensation. The pressure drop during the expansion, Δp, determines changes in temperature and the partial pressure of water vapor during the expansion. These factors combine to control changes in S and lead to an estimated maximum S_{max} above 3 or 4 for a typical

09 May 2025 20:58:15

© Author(s) 2025

expansion experiment. As such, it is reasonable to assume that all seeding aerosols will be activated and nucleate droplets during an expansion, causing C_{drop} to track directly with C_0.

Figure 11 shows a plot of C_{drop} calculated from Eq. (13) as a function of C_0 for all initial S_0 and mixing conditions. Error bars on measurements of C_{drop} derive from uncertainties in τ_f and $\mathscr{U}_{rms}$. At intermediate concentrations (4×10^3 #/cm^3 < C_0 < 8×10^4 #/cm^3), C_{drop} falls close to the gray dashed line, which has a slope of $C_{drop}/C_0 = 1$, suggesting that every solid aerosol in the chamber nucleates a droplet during the expansion.

The curves of C_{drop} do deviate from this 1:1 line for both low and high values of C_0. Deviations at lower aerosol concentrations ($C_0 < 4 \times 10^3$ #/cm^3) could be related to larger PDA measurement errors at lower particle counts, as well as related uncertainties in estimating the cloud lifetime (see Fig. 8). At high aerosol concentrations ($C_0 > 8 \times 10^4$ #/cm^3), the concentration of droplets observed undershoots the concentration of seeding aerosols, i.e., not all aerosol particles are activated. This suggests that for high C_0, rapid water condensation onto numerous, easily activated particles keeps the actual S in the chamber very close to 1, preventing the activation of less efficient condensation nuclei in the aerosol distribution. Experimental uncertainties could also be partly responsible for $C_{drop} < C_0$ at high C_0: PDA is only sensitive to droplets larger than 1 μm, so if smaller droplets are present, they would be missed by this analysis. Indeed (as detailed further below), when more droplets are formed, they are smaller on average, due to conservation of mass. Results with and without forced mixing are similar, suggesting that the fans do not act as droplet impactors or induce significant loss of droplets.

The mass of liquid water per unit volume that condenses following an expansion can be estimated as

$$\mathscr{L} = q_l \rho_f = \frac{\pi \overline{d}^3}{6} C_{drop} \rho_w, \tag{14}$$

where q_l is the specific liquid water content (kg liquid water/kg humid air) of the air parcel after the expansion, ρ_f is the density of the air parcel after the expansion, and ρ_w is the density of liquid water. ρ_f can be found with the ideal gas law as $\rho_f = p_f/(R_d T_f)$. q_l is given by $q_l = S_0 q^*(T_0, p_0) - q^*(T_f, p_f)$ from the conservation of total water (both liquid and vapor) and can be estimated using the expression for q^* in Eq. (9). From Eq. (14), we see that the total mass of liquid water will scale as $C_{drop} \times \overline{d}^3$. This implies that when many droplets are formed, they will tend to be smaller.

From Eq. (14), we also have $\overline{d} \propto \mathscr{L}^{1/3}$. Taking $C_{drop} \approx C_0$, we can rearrange Eq. (14) to find that

$$\overline{d} = \left(\frac{6 q_l \rho_f}{\pi C_{drop} \rho_w} \right)^{1/3} \approx \left(\frac{6 q_l \rho_f}{\pi C_0 \rho_w} \right)^{1/3}. \tag{15}$$

The three red dashed lines in Fig. 10(b) represent least-square linear regression fits of the function $\overline{d} = \mathscr{F} C_0^{-1/3}$ to our experimental data, with good agreement.

We can qualitatively compare the droplet size scaling with C_0 to the work of Shaw *et al.*[50] in the context of Π chamber experiments. The Π chamber operates under statistically steady-state conditions, with a constant aerosol injection rate of $\dot{n}_{inj}$, compensated by wall loss and sedimentation. The mean droplet size $\overline{d}$ is then related to the rate of droplet nucleation, which is assumed to be proportional to the injection rate, yielding $\overline{d} \propto \dot{n}_{inj}^{-1/3}$. In our REACh chamber, the expansion is a transient phenomenon. However, if we assume $\dot{n}_{inj} \propto C_0$, our scaling argument for the droplet size with aerosol concentration given in Eq. (15) and our data (Fig. 10) agree with the steady state results of Shaw *et al.*[50] We also note that the range of aerosol and droplet concentrations explored in the Π chamber[51,52] ranges from 2 to 2.2 10^4 #/cm^3, with a significant overlap with the experimental conditions presented here. This point of comparison provides confidence that our ability to rapidly probe a range of experimental conditions with the REACh facility can provide useful physical insights into cloud microphysics.

D. Holographic measurements of nucleation onset and droplet growth

Finally, we demonstrate the capabilities of holography for tracking droplet nucleation and growth. Our holographic system has the advantage of being able to probe a much larger measurement volume than PDA. Holography measurements average over a path length spanning the chamber and can, therefore, access more dilute regimes, closer to nucleation threshold and more relevant to the droplet concentrations observed in actual clouds. It is important to note that thanks to the large sampling volume (8.44 cm^3), the holographic system measures more individual droplets than PDA and achieves better statistics, allowing us to track the droplet size distribution in time.

In Fig. 12, we report the temporal evolution of the droplet size distribution tracked with holography for a single expansion. Figure 12(b) plots the number of drops detected, Fig. 12(c) plots the mean droplet diameter, and Fig. 12(d) shows the droplet size distribution. The experiment is performed with an initial saturation ratio of $S_0 = 0.3$, an initial aerosol concentration of $C_0 = 71$ #/cm^3, and a pressure drop of $\Delta p = 0.36$ bar under unforced mixing conditions. The minimum temperature reached is close to −16 °C [Fig. 12(a)]. This combination of Δp and S_0 is chosen to be relatively close to the threshold of droplet nucleation, while we work with a low concentration of seeding aerosols to avoid excessively high droplet concentrations that can obscure the holographic data.

The first droplets are detected by holography ∼1 s after the temperature drop. In a first regime, occurring 1–2.5 s after expansion, we observe a rapid increase in the number of droplets detected in the measurement volume up to 10^4 per time bin [Fig. 12(b)], together with an increase in the mean droplet diameter up to 20 μm [Figs. 12(c) and 12(d)]. The mean droplet diameter appears to grow as $\sqrt{t}$, consistent with diffusive growth. We note that droplets larger than 20–25 μm are most likely to grow through collisions and coalescence instead of diffusive growth; see the discussion by Poydenot and Andreotti.[8] After 2–3 s, the droplet number plateaus before slowly decreasing, while the mean diameter continues to increase until $t \sim 6$ s. The concentration of liquid droplets is calculated by dividing the number of measured droplets by the holography measurement volume (8.44 cm^3). The maximum droplet concentration is ∼22 ± 2.1#/cm^3 and is reached at $t = 2.0$ s, during the first droplet growth regime. The maximum droplet concentration

09 May 2025 20:58:15

© Author(s) 2025

is on the same order of magnitude as the concentration of seeding aerosols.

These findings highlight our ability to directly measure the growth of droplets during an expansion using holography in dilute regimes. We note that the absolute number of droplets detected here is much higher than when using PDA in Sec. III C 3 because of the much larger detection volume, while the actual droplet concentration is smaller. Overall, our combined use of PDA and holography allows us to probe droplet nucleation and growth over a wide range of conditions.

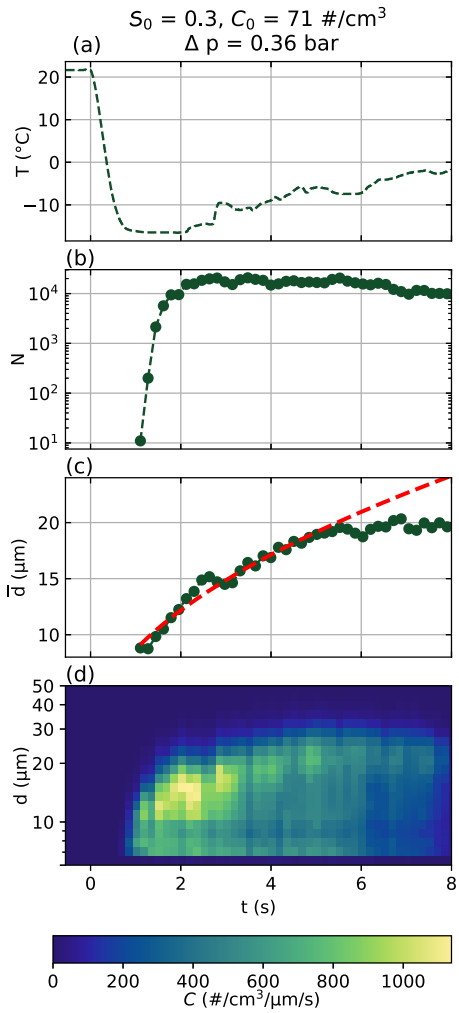

FIG. 12. Time evolution of the (a) temperature, (b) droplet number, (c) mean droplet diameter, and (d) droplet size distribution during an expansion with $S_0 = 0.3$, $C_0 = 71$ #/cm^3, and $\Delta p = 0.36$ bar. Droplet numbers and diameters are recorded using inline holography recording at 600 Hz. The expansion is triggered at $t = 0$ s. The thermodynamic conditions in the chamber are close to the onset of droplet nucleation. The time bins in panels (b) and (c) are spaced with $\Delta t = 0.17$ s. The red line in panel (c) shows a fit to the droplet diameter data from $t = 1.2$ to 5.5 s of the function $d(t) = \sqrt{d_0^2 + a(t - t_0)}$, where $d_0 = 6$ μm, $t_0 = 0.5$ s, and $a = 73$ m^2/s. The color map in panel (d) shows the concentration of droplets in each bin, C, per unit volume, per micrometer, per second.

IV. CONCLUSIONS

We have presented a new experimental rapid expansion cloud chamber facility designed to study processes relevant to aerosols and cloud microphysics. The experimental principle of our facility is that of an expansion chamber but with the addition of state-of-the-art real-time diagnostics and the ability to induce turbulent flows. The experimental facility comprises two vacuum-sealed chambers, which are capable of reproducing an adiabatic-like expansion, where the gas from the aerosol-nucleation chamber is allowed to expand into the evacuated expansion chamber, causing a sudden increase in saturation ratio. We demonstrate precise control over the initial conditions of the expansion, including the initial saturation ratio, S_0, seeding aerosol concentration, C_0, and air mixing conditions.

Our facility design allows us to achieve a high repetition rate of experiments to probe a wide range of conditions and ample optical access to perform high frequency real-time measurements. This report represents an initial demonstration of these capabilities. First, we characterize the chamber thermodynamics, finding the minimum temperature during the expansion in good agreement with theoretical predictions for both dry and moist conditions. We then present a discussion of droplet nucleation and growth in the presence of seeding aerosol particles for a range of experimental parameters. We characterize the total droplet number and mean droplet diameter throughout expansions. We observe the classic competition between the number of droplets and droplet size for a fixed amount of water vapor; the more the seeding aerosol, the more the droplets are observed and the smaller they are on average. The droplet concentration is shown to scale linearly with the initial aerosol concentration, while the mean droplet size decreases with seeding aerosol concentration. Simple scaling laws based on thermodynamic principles can describe these trends. Finally, we demonstrate the ability to characterize droplet growth under conditions near the onset of nucleation using inline holography.

The key advantage of the REACh facility is our high experimental repetition rate and our use of high-speed measurement techniques that enable us to conduct systematic parametric studies more efficiently than larger facilities. Future studies will involve detailed investigations of the interplay of homogeneous and heterogeneous droplet nucleation. We are also implementing high-speed infrared absorption measurements to directly measure the changing water vapor concentration (and therefore saturation ratio) throughout each expansion, coincident with holography measurements. We will also consider the role of turbulent mixing of different intensities and anisotropies. Finally, the chamber walls are equipped with a cooling system, which will permit us to explore lower-temperature conditions and the nucleation and growth of ice crystals in future work.

SUPPLEMENTARY MATERIAL

The supplementary material includes engineering drawings of the aerosol chamber and the expansion chamber.

ACKNOWLEDGMENTS

This work was supported by a seed grant from the Simons Foundation (Award No. 1019423) and Princeton University internal

09 May 2025 20:58:15

© Author(s) 2025

funds from the Princeton Catalysis Initiative and the High Meadows Environmental Institute's Climate and Energy Grand Challenge Award granted to L.D. and M.L.W. We thank Clare Singer for performing the internal review of this manuscript for NOAA-GFDL.

AUTHOR DECLARATIONS

Conflict of Interest

The authors have no conflicts to disclose.

Author Contributions

Martin A. Erinin: Conceptualization (equal); Data curation (equal); Formal analysis (equal); Investigation (equal); Methodology (equal); Software (equal); Supervision (equal); Validation (equal); Visualization (equal); Writing – original draft (equal); Writing – review & editing (equal). **Cole R. Sagan**: Data curation (equal); Formal analysis (equal); Investigation (equal); Methodology (equal); Software (equal); Validation (equal); Writing – review & editing (equal). **Ilian Ahmed**: Data curation (equal); Formal analysis (equal); Investigation (equal); Methodology (equal); Validation (equal); Visualization (equal); Writing – original draft (equal); Writing – review & editing (equal). **Gwenore F. Pokrifka**: Data curation (equal); Formal analysis (equal); Investigation (equal); Writing – review & editing (equal). **Nadir Jeevanjee**: Formal analysis (equal); Investigation (equal); Methodology (equal); Visualization (equal); Writing – original draft (equal); Writing – review & editing (equal). **Marissa L. Weichman**: Conceptualization (equal); Formal analysis (equal); Funding acquisition (equal); Methodology (equal); Project administration (equal); Resources (equal); Supervision (equal); Validation (equal); Writing – original draft (equal); Writing – review & editing (equal). **Luc Deike**: Conceptualization (equal); Formal analysis (equal); Funding acquisition (equal); Investigation (equal); Methodology (equal); Project administration (equal); Resources (equal); Supervision (equal); Validation (equal); Writing – original draft (equal); Writing – review & editing (equal).

DATA AVAILABILITY

All data used in preparing this work are available upon request.

REFERENCES

[1]K. Calvin, D. Dasgupta, G. Krinner, A. Mukherji, P. Thorne, C. Trisos, J. Romero, P. Aldunce, K. Barrett, G. Blanco *et al.*, in *Contribution of Working Groups I, II and III to the Sixth Assessment Report of the Intergovernmental Panel on Climate Change* (IPCC, 2023), p. 1.
[2]S. J. Ghan, H. Abdul-Razzak, A. Nenes, Y. Ming, X. Liu, M. Ovchinnikov, B. Shipway, N. Meskhidze, J. Xu, and X. Shi, J. Adv. Model. Earth Syst. **3**, 1–33 (2011).
[3]J. H. Seinfeld and S. N. Pandis, *Atmospheric Chemistry and Physics* (European Geosciences Union, Copernicus Publications, 1998), p. 1326.
[4]H. R. Pruppacher, J. D. Klett, and P. K. Wang, *Microphysics of Clouds and Precipitation* (Taylor & Francis, 1998).
[5]E. Bodenschatz, S. P. Malinowski, R. A. Shaw, and F. Stratmann, Science **327**, 970 (2010).
[6]P. Prabhakaran, A. S. M. Shawon, G. Kinney, S. Thomas, W. Cantrell, and R. A. Shaw, Proc. Natl. Acad. Sci. U. S. A. **117**, 16831 (2020).
[7]J. M. Yeom, I. Helman, P. Prabhakaran, J. C. Anderson, F. Yang, R. A. Shaw, and W. Cantrell, Proc. Natl. Acad. Sci. U. S. A. **120**, e2307354120 (2023).
[8]F. Poydenot and B. Andreotti, Phys. Rev. Fluids **9**, 123602 (2024).
[9]S. M. Burrows, C. S. McCluskey, G. Cornwell, I. Steinke, K. Zhang, B. Zhao, M. Zawadowicz, A. Raman, G. Kulkarni, S. China *et al.*, Rev. Geophys. **60**, e2021RG000745, https://doi.org/10.1029/2021rg000745 (2022).
[10]T. Storelvmo, Annu. Rev. Earth Planet. Sci. **45**, 199 (2017).
[11]Z. A. Kanji, L. A. Ladino, H. Wex, Y. Boose, M. Burkert-Kohn, D. J. Cziczo, and M. Krämer, Meteorol. Monogr. **58**, 1.1–1.33 (2017).
[12]C. Hoose and O. Möhler, Atmos. Chem. Phys. **12**, 9817 (2012).
[13]G. Feingold, V. P. Ghate, L. M. Russell, P. Blossey, W. Cantrell, M. W. Christensen, M. S. Diamond, A. Gettelman, F. Glassmeier, E. Gryspeerdt *et al.*, Sci. Adv. **10**, eadi8594 (2024).
[14]U. Lohmann and B. Gasparini, Science **357**, 248 (2017).
[15]B. J. Mason, Contemp. Phys. **4**, 27 (1962).
[16]J. L. Schmitt, J. L. Kassner, Jr., and J. Podzimek, J. Aerosol Sci. **13**, 373 (1982).
[17]R. C. Miller, R. J. Anderson, J. L. Kassner, Jr., and D. E. Hagen, J. Chem. Phys. **78**, 3204 (1983).
[18]R. A. Shaw, Annu. Rev. Fluid Mech. **35**, 183 (2003).
[19]R. A. Shaw, W. Cantrell, S. Chen, P. Chuang, N. Donahue, G. Feingold, P. Kollias, A. Korolev, S. Kreidenweis, S. Krueger *et al.*, Bull. Am. Meteorol. Soc. **101**, E1026 (2020).
[20]R. Wagner, C. Linke, K.-H. Naumann, M. Schnaiter, M. Vragel, M. Gangl, and H. Horvath, J. Quant. Spectrosc. Radiat. Transfer **110**, 930 (2009).
[21]K. Chang, J. Bench, M. Brege, W. Cantrell, K. Chandrakar, D. Ciochetto, C. Mazzoleni, L. R. Mazzoleni, D. Niedermeier, and R. A. Shaw, Bull. Am. Meteorol. Soc. **97**, 2343 (2016).
[22]F. Vogel, L. Lacher, J. Nadolny, H. Saathoff, T. Leisner, and O. Möhler, Rev. Sci. Instrum. **93**, 095106 (2022).
[23]O. Möhler, M. Adams, L. Lacher, F. Vogel, J. Nadolny, R. Ullrich, C. Boffo, T. Pfeuffer, A. Hobl, M. Weiß *et al.*, Atmos. Meas. Tech. Discuss. **2020**(14), 1143–1166 (2021).
[24]F. Vogel, M. P. Adams, L. Lacher, P. B. Foster, G. C. E. Porter, B. Bertozzi, K. Höhler, J. Schneider, T. Schorr, N. S. Umo *et al.*, Atmos. Chem. Phys. **24**, 11737 (2024).
[25]C. Graziani, M. Nespoulous, R. Denoyel, S. Fauve, C. Chauveau, L. Deike, and M. Antoni, C. R. Mec. **351**, 183 (2023).
[26]R. L. McGraw, P. M. Winkler, and P. E. Wagner, Sci. Rep. **7**, 16896 (2017).
[27]P. E. Wagner, D. Kaller, A. Vrtala, A. Lauri, M. Kulmala, and A. Laaksonen, Phys. Rev. E **67**, 021605 (2003).
[28]R. A. Shaw, W. C. Reade, L. R. Collins, and J. Verlinde, J. Atmos. Sci. **55**, 1965 (1998).
[29]A. B. Kostinski and R. A. Shaw, J. Fluid Mech. **434**, 389 (2001).
[30]N. J. Bacon, M. B. Baker, and B. D. Swanson, Q. J. R. Metereol. Soc. **129**, 1903 (2003).
[31]G. F. Pokrifka, A. M. Moyle, L. E. Hanson, and J. Y. Harrington, J. Atmos. Sci. **77**, 2393 (2020).
[32]G. F. Pokrifka, A. M. Moyle, and J. Y. Harrington, J. Atmos. Sci. **80**, 501 (2023).
[33]H. Bocanegra Evans, N. Dam, G. Bertens, D. van der Voort, and W. van de Water, Phys. Rev. Lett. **117**, 164501 (2016).
[34]G. H. Good, P. J. Ireland, G. P. Bewley, E. Bodenschatz, L. R. Collins, and Z. Warhaft, J. Fluid Mech. **759**, R3 (2014).
[35]J. P. Fugal and R. A. Shaw, Atmos. Meas. Tech. **2**, 259 (2009).
[36]M. A. Erinin, B. Néel, M. T. Mazzatenta, J. H. Duncan, and L. Deike, Exp. Fluids **64**, 96 (2023).
[37]M. A. Beals, J. P. Fugal, R. A. Shaw, J. Lu, S. M. Spuler, and J. L. Stith, Science **350**, 87 (2015).
[38]D. W. Fahey, R.-S. Gao, O. Möhler, H. Saathoff, C. Schiller, V. Ebert, M. Krämer, T. Peter, N. Amarouche, L. M. Avallone *et al.*, Atmos. Meas. Tech. **7**, 3177 (2014).
[39]B. Buchholz, A. Afchine, and V. Ebert, Atmos. Meas. Tech. **7**, 3653 (2014).
[40]R. C. Sullivan, M. J. K. Moore, M. D. Petters, S. M. Kreidenweis, G. C. Roberts, and K. A. Prather, Atmos. Chem. Phys. **9**, 3303 (2009).

09 May 2025 20:58:15

© Author(s) 2025

[41] H. N. Huynh and V. F. McNeill, ACS Earth Space Chem. **5**, 1896 (2021).
[42] M. Tang, D. J. Cziczo, and V. H. Grassian, Chem. Rev. **116**, 4205 (2016).
[43] J. T. Pasquier, J. Henneberger, A. Korolev, F. Ramelli, J. Wieder, A. Lauber, G. Li, R. O. David, T. Carlsen, R. Gierens *et al.*, Geophys. Res. Lett. **50**, e2022GL100247, https://doi.org/10.1029/2022gl100247 (2023).
[44] M. Yau and R. Rogers, *A Short Course in Cloud Physics* (Elsevier Science, 1996).
[45] D. M. Romps, J. Atmos. Sci. **74**, 3891 (2017).
[46] D. M. Romps, J. Atmos. Sci. **73**, 3719 (2016).
[47] J. Latham and R. L. Reed, Q. J. R. Metereol. Soc. **103**, 297 (1977).
[48] M. B. Baker, R. G. Corbin, and J. Latham, Q. J. R. Metereol. Soc. **106**, 581 (1980).
[49] F. Hoffmann and G. Feingold, J. Atmos. Sci. **76**, 1955 (2019).
[50] R. A. Shaw, S. Thomas, P. Prabhakaran, W. Cantrell, M. Ovchinnikov, and F. Yang, Phys. Rev. Res. **5**, 043018 (2023).
[51] K. K. Chandrakar, W. Cantrell, K. Chang, D. Ciochetto, D. Niedermeier, M. Ovchinnikov, R. A. Shaw, and F. Yang, Proc. Natl. Acad. Sci. U. S. A. **113**, 14243 (2016).
[52] T. MacMillan, R. A. Shaw, W. H. Cantrell, and D. H. Richter, Phys. Rev. Fluids **7**, 020501 (2022).

09 May 2025 20:58:15

© Author(s) 2025